



Atmospheric Cold Pools in the Bay of Bengal

IURY T. SIMOES-SOUSA¹,^a AMIT TANDON²,^a JARED BUCKLEY,^a DEBASIS SENGUPTA,^b SREE LEKHA J.,^c
EMILY SHROYER,^d AND SIMON P. DE SZOEKE^d

^a *University of Massachusetts Dartmouth, North Dartmouth, Massachusetts*

^b *Centre for Atmospheric and Oceanic Sciences, Indian Institute of Science, Bangalore, India*

^c *NOAA/Pacific Marine Environmental Laboratory, Seattle, Washington*

^d *Oregon State University, Corvallis, Oregon*

(Manuscript received 2 February 2022, in final form 25 July 2022)

ABSTRACT: Atmospheric cold pools, generated by evaporative downdrafts from precipitating clouds, are ubiquitous in the Bay of Bengal. We use data from three moorings near 18°N to characterize a total of 465 cold pools. The cold pools are all dry, with a typical temperature drop of 2°C (maximum 5°C) and specific humidity drop of 1 g kg⁻¹ (maximum = 6 g kg⁻¹). Most cold pools last 1.5–3.5 h (maximum = 14 h). Cold pools occur almost every day in the north bay from April to November, principally in the late morning, associated with intense precipitation that accounts for 80% of total rain. They increase the latent heat flux to the atmosphere by about 32 W m⁻² (median), although the instantaneous enhancement of latent heat flux for individual cold pools reaches 150 W m⁻². During the rainiest month (July), the cold pools occur 21% of the time and contribute nearly 14% to the mean evaporation. A composite analysis of all cold pools shows that the temperature and specific humidity anomalies are responsible for ~90% of the enhancement of sensible and latent heat flux, while variations in wind speed are responsible for the remainder. Depending on their gust-front speed, the estimated height of the cold pools primarily ranges from 850 to 3200 m, with taller fronts more likely to occur during the summer monsoon season (June–September). Our results indicate that the realistic representation of cold pools in climate models is likely to be important for improved simulation of air–sea fluxes and monsoon rainfall.

SIGNIFICANCE STATEMENT: Atmospheric cold pools form over the ocean when falling rain evaporates, leading to a dense cold air mass spreading over the surface. They impact air–sea heat exchanges over tropical regions and give rise to new rainstorms. We analyze data from three fixed, closely spaced buoys to describe cold pools and investigate their role in rainfall and air–sea interactions in the northern Bay of Bengal (Indian Ocean). We find that cold pools are associated with about 80% of all rain and are important for ocean–atmosphere heat and moisture exchange, especially from April to November. We estimate the speed of cold pools and derive their heights (850–3200 m) using theory.

KEYWORDS: Atmosphere; Ocean; Atmosphere–ocean interaction; Cold pools; Surface fluxes

1. Introduction

Atmospheric cold pools are cold pockets of air formed in downdrafts by the evaporative cooling of clouds or raindrops (Charba 1974; Goff 1976; Zipser 1977; Black 1978). These cold downdrafts expand horizontally upon reaching the surface, lasting for a few hours while forming gust fronts that reinitiate convective processes, resulting in more rain. Mechanical lifting of warm moist air at the edges of the cold pool fronts triggers new precipitating convective cells (see Fig. 2 from Goff 1976). In addition, other evidence has proposed that the accumulated water vapor at the edge of cold pools can provide enough buoyancy to trigger new convection (Tompkins 2001). More recently, numerical simulations have suggested that the mechanical lifting elevates parcels from the surface, while

thermodynamic forcing reduces the inhibition parcels experience before reaching free convection (Torri et al. 2015).

Cold pools can be very strong despite being transient (few hours) and considerably smaller than their parent mesoscale storms. A remarkable example of one such event was seen on 26 August 2015, during the first leg of the Air–Sea Interaction Research Initiative (ASIRI) cruise. The R/V *Roger Revelle* scientific party was crossing the Bay of Bengal at 13°N when they felt the air temperature suddenly drop more than 5°C in 10 min, followed by gusty winds with fluctuating direction. Massive clouds blocked most of the sunlight at this time, accompanied by an intense rainfall (maximum value ~ 16 mm h⁻¹) that lasted for hours. The meteorological station data of the ship confirm the passage through an atmospheric cold pool (Fig. 1).

Numerical simulations have shown that the specific humidity of land-based cold pools strongly depends on the soil moisture, with taller moist cold pools forming over dry soils and shorter dry cold pools forming over wet soils (Drager et al. 2020),

Corresponding author: Amit Tandon, atandon@umassd.edu

DOI: 10.1175/JAS-D-22-0041.1

© 2022 American Meteorological Society. For information regarding reuse of this content and general copyright information, consult the AMS Copyright Policy (www.ametsoc.org/PUBSReuseLicenses).

Brought to you by University of Maryland, McKeldin Library | Unauthenticated | Downloaded 07/27/23 08:16 PM UTC

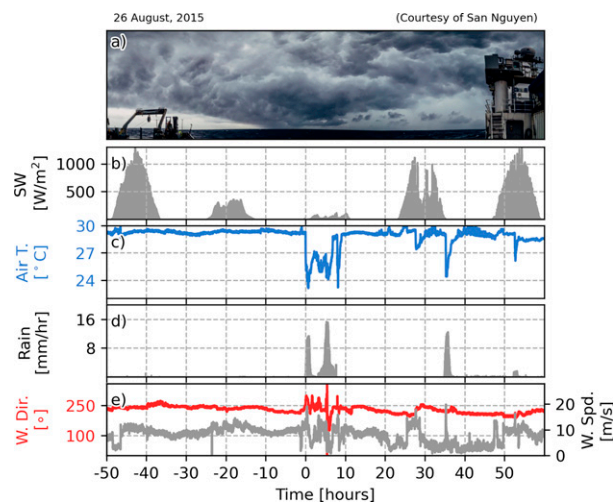


FIG. 1. (a) Storm clouds seen from R/V *Roger Revelle*. Four days of 1-min measurements from shipboard meteorological station for (b) incident shortwave radiation (W m^{-2}), (c) air temperature ($^{\circ}\text{C}$), (d) rainfall (mm h^{-1}), and (e) wind direction (degrees; red) and wind speed (m s^{-1} ; gray). Early on 26 Aug 2015, air temperature fell by more than 5°C in 10 min. Photo courtesy: San Nguyen.

although convective cloud organization could also play a role in the moisture content of the cold pools (de Szoeko et al. 2017). Over the ocean, cold pools are usually dry and substantially affect the air–sea fluxes (de Szoeko et al. 2017; Joseph et al. 2021). Another interesting aspect is that modeled dry cold pools frequently present a moist ring at the leading edge, which could be explained by either the expanding cold pool at the center of the moist air from the parent storm, or by the enhanced evaporation at the cold pool front (Tompkins 2001; Langhans and Roms 2015; Drager et al. 2020).

Cold pools are important for the air–sea fluxes. For instance, de Szoeko et al. (2017) show that equatorial oceanic cold pools are considerably dry, enhancing latent heat flux by 25 W m^{-2} (20% of the mean) and sensible heat flux by 9 W m^{-2} (100%). In the Bay of Bengal, cold pools enhance surface fluxes even more. Joseph et al. (2021) show that cold pools south of 15°N in the Bay of Bengal enhance the latent heat flux by 70 W m^{-2} and the sensible heat flux by 28 W m^{-2} on average, with an important latitudinal variability. Cold pools are also important for the wind-driven mixing of diurnal warm layers and sea surface temperature in the Bay of Bengal (Girishkumar et al. 2021).

Alongside their frequency of occurrence, the distribution of the size of cold pools is also essential for understanding their role in weather and climate predictions. Unfortunately, cold pools are difficult and expensive to survey—especially over the ocean—due to their transience and small scale. So far, few researchers have addressed the problem of the estimation of cold pools’ size and height using observations (Terai and Wood 2013; Zuidema et al. 2017; de Szoeko et al. 2017; van den Heever et al. 2021). Most of the works employ numerical simulations and focus on land-based cold pools (Dawson et al. 2010; Li et al. 2014; Jeevanjee 2017; Mallinson and

Lasher-Trapp 2019; Drager et al. 2020). However, Grant and van den Heever (2016) show that for experiments with different grid spacing, the same initial cold pocket of air affects the surface heat flux differently, which consequently expands to different of length scales. Their study suggests that at least a 100 m horizontal resolution is needed to simulate cold pools correctly.

Different studies have explored different data sampling approaches and aspects of cold pools over the ocean. For instance, Terai and Wood (2013) observed cold pools by aircraft measurement, Zuidema et al. (2017) by satellite, and de Szoeko et al. (2017) by oceanographic and meteorological cruises. More recently, van den Heever et al. (2021) observed land-based cold pools using drones, and Wills et al. (2021) observed ocean-based cold pools using saildrones. To our knowledge, until now, there is no study that estimates the height and propagation of cold pool fronts in the north Bay of Bengal, an important region for genesis of monsoon tropical depressions (e.g., Goswami et al. 2016).

The main goal of this study is to investigate the atmospheric cold pools in the north Bay of Bengal. To address this objective, we formulate the following specific questions:

- What are the characteristics of the atmospheric cold pools?
- What is their contribution to the air–sea fluxes and association with total rain?
- What is their temporal variability, and what is their height distribution?

In section 2, we describe the study region and the dataset. Section 3 details the method of identification of cold pools from mooring data and section 4 describes the basic statistics of the cold pool events in the Bay of Bengal. In section 5, we discuss the impact of the cold pools on the air–sea fluxes, present composites in section 6. In section 7, we describe how we estimate the height of the cold pools by matching propagating fronts observed at three different moorings, and conclude with section 8.

2. The dataset

The study region of our analyses is the northern Bay of Bengal (Indian Ocean), where three different moorings—BD08, BD09, and WHOI—sampled atmospheric and oceanographic data simultaneously in 2015 (Fig. 2a). The Indian National Institute of Ocean Technology (NIOT) collected and provided the data from BD08 and BD09 moorings and the Woods Hole Oceanographic Institution installed the WHOI mooring and provided the data. The three moorings are located approximately at 18°N , 89.6°E . The BD08 and BD09 are 34 km apart from each other (29 km between WHOI and BD08, and 31 km between WHOI and BD09). We uniquely capture the propagation of cold pools’ fronts, for those larger than the distance between moorings.

The 1-min time series of the air temperature is very similar between different moorings (Figs. 2b–d): all show remarkable sharp drops of more than 1°C h^{-1} (red) from the 30-day running-average series (gray). These sharp drops happen frequently from late April to November, and as expected by their proximity, the sharp drops seem to be almost simultaneous

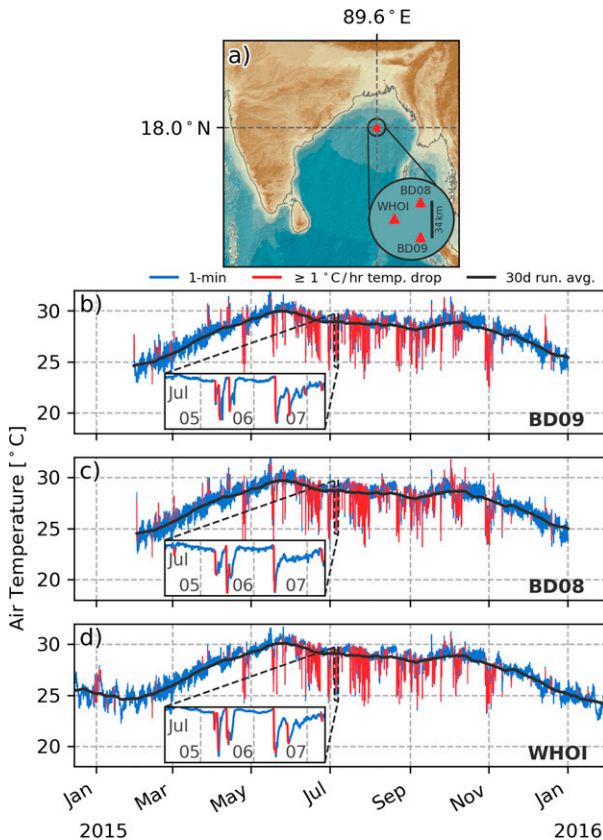


FIG. 2. (a) Map with the location of the moorings. Air temperature (°C) time series for (b) BD08, (c) BD09, and (d) WHOI moorings. The red lines are for $\geq 1^{\circ}\text{C h}^{-1}$ of temperature drop, and the gray lines represent the 30-day running average. Map based on Cherian et al. (2020).

at the three moorings. Most of the events happen during the summer monsoon season. Moreover, the zoomed panels show that temperature drops of different durations are usually stacked into multiple events at the same time of the day.

So far, we have described some of the characteristics of sharp temperature drops possibly related to cold pools from the visible patterns in the time series. We next consider the automatic identification of cold pools.

3. Identifying cold pools from mooring data

We characterize cold pools by their sharp air temperature drops, usually greater than 1°C h^{-1} (de Szoek et al. 2017). Based on this threshold from observations and previous work, we choose a method that uses both the air temperature and its time derivative to identify cold pool events in the mooring data. We define prominence for air temperature as the range (in $^{\circ}\text{C}$) between the local minimum¹ and the highest local maximum that does not enclose deeper negative peaks (Fig. 3, right panels). The detection method is described below:

¹Local minimum: $T_{i-1} > T_i < T_{i+1}$. Local maximum: $T_{i-1} < T_i > T_{i+1}$.

- 1) remove the 30-day running average from air temperature data (gray line from Figs. 2b–d),
- 2) find all negative peaks with prominence $\geq 0.5^{\circ}\text{C}$, and
- 3) keep only peaks with a $\geq 1^{\circ}\text{C h}^{-1}$ temperature drop over 1 h.

This method is based on the definition for topographic prominence, commonly used in geography (Llobera 2001). The closest local maximum that satisfies this criterion is then used to define the duration of a cold pool event. This method identifies cold pools without needing any previous assumptions about the duration or interval between different peaks. We note that the temperature drops occur very close to each other many times, and last for different periods in the mooring time series (Fig. 2). The last step of the algorithm distinguishes cold pools from regular nighttime cooling.

All identified cold pools are marked in red for each mooring presented in Fig. 3. Despite missing a few events—identified by visual inspection—the method correctly identifies the cold pool events. To test the sensitivity of this method, we vary the minimum required prominence from 0.2° to 0.8°C , which varies the number of cold pools from 471 to 443, and hence is relatively insensitive. We also vary the minimum temperature drop and time threshold from 0.5° to $1.5^{\circ}\text{C h}^{-1}$ (hours for the time threshold), which varies the number of cold pools from 477 to 432. The number of cold pools is also very similar between the moorings for all the values tested. Therefore, we characterize the identified cold pools using a 0.5°C prominence and a 1°C h^{-1} temperature drop for the remainder of this paper.

4. The duration of cold pools

Cold pool temperature drops are usually not symmetrical in time, with a leading front marked by a sharp temperature drop in the beginning and slower recovery time, and most of the previous studies have characterized cold pool recovery time (de Szoek et al. 2017; Joseph et al. 2021). There are different definitions of recovery time in the literature. However, in theory, the recovery time is the time it takes for the minimum temperature to recover to the background temperature before the front. Mixing and advecting processes usually change the background temperature, and most of the observations show that the recovered temperature is colder than the prefront temperature (de Szoek et al. 2017; Wills et al. 2021). Similar to the occurrence and the total number of cold pools, the distribution of cold pools’ recovery time is also very similar between different moorings (Fig. 4).

The positively skewed cumulative density function (CDF) highlights that cold pool events typically spanned 1.5–3.5 h (60%), but some events lasted up to 10 h. Their distribution is approximately lognormal (see gray line, Fig. 4) with a median of ~ 2 h and skewness of ~ 2.0 . That means that the cold pools we identify in the north Bay of Bengal last substantially longer than equatorial cold pools (~ 0.5 h of median recovery time; de Szoek et al. 2017). Joseph et al. (2021) have shown that cold pools last shorter closer to the equator, with ~ 1.0 h of median recovery time at 8°N and ~ 1.3 h of median recovery time at 15°N . Our analyses suggest longer recovery time

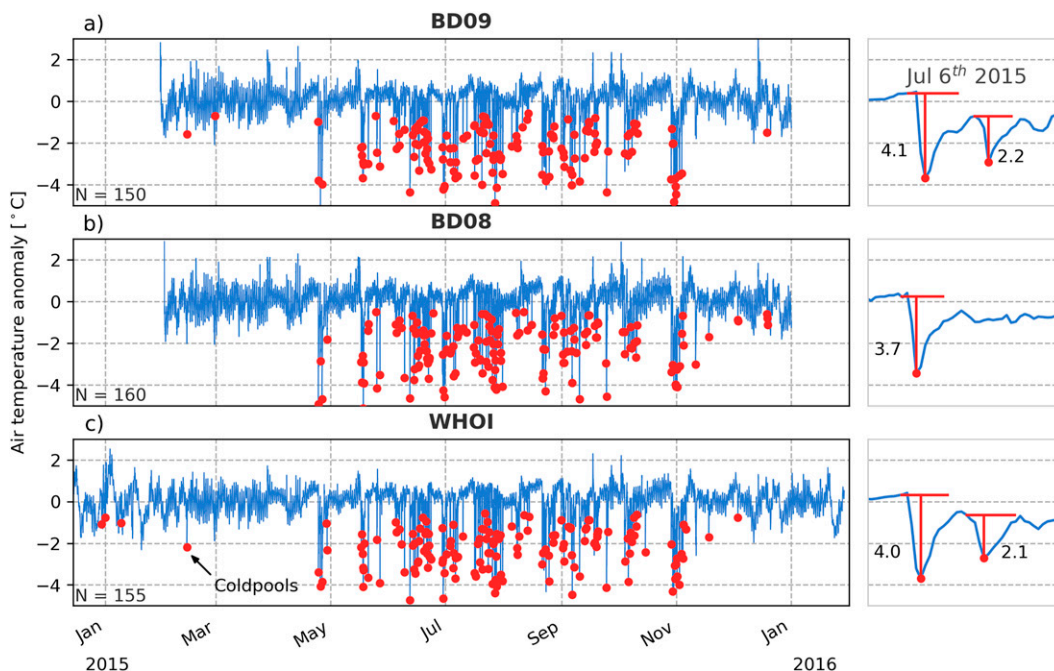


FIG. 3. (left) Time series of the air temperature anomaly from (a) BD09, (b) BD08, and (c) WHOI. The red dots represent the negative peak of the identified cold pools. (right) Zoomed-in time series with cold pools' prominence (numbers) for 6 Jul 2015 (18 h from 0500 to 1100 local time).

for cold pools at 18°N . Note that this result also reaffirms the choice of our detection method, which does not make any assumptions about the duration of events.

5. Air–sea fluxes and rain during cold pools

We demonstrate the association of cold pools with air–sea fluxes and rain by choosing a 10-day time range during the rainiest season as an example (Fig. 5a). Most of the striking peaks in the rain rate occur within cold pools, supporting the strong relationship between cold pools and rain events (shared area, Fig. 5a). In fact, this pattern occurs even beyond the selected time range, and $\sim 80\%$ of the total rain in the whole time series occurs within cold pools, pointing out the major importance of cold pools for rainfall in the Bay of Bengal.

It is also impressive that the patterns of the precipitation from 30-min Integrated Multi-satellite Retrievals for GPM (IMERG) data smoothly follow the cold pool events (red line, Fig. 5a). The Pearson's correlation coefficient between IMERG and WHOI is 87%, for the total daily rain, which suggests that IMERG correctly represents most of the daily rain variability from the mooring data. Despite missing the amplitude of the rain events, sometimes by an order of magnitude, the IMERG total rain in the whole time series is 23% higher than in mooring data. This result may be related to the analysis presented by Thakur et al. (2020), which suggests that IMERG overestimates the rain rate during extreme storms, missing the smaller-scale variability ($<1/4^{\circ}$). While the rain patterns may not follow the cold pool boundaries, the IMERG product seems appropriate for tracking the rain associated with cold pools in the Bay of Bengal.

In addition to the remarkable signature in the rain-rate patterns, the cold pools also strongly influence the latent and sensible heat fluxes in the Bay of Bengal (Figs. 5b,c) as computed using the Coupled Ocean–Atmosphere Response Experiment bulk parameterization model version 3.5 (hereafter COARE 3.5; Fairall et al. 1996, 2003; Edson et al. 2013). For the chosen time range, cold pools can enhance the sensible sea surface heat loss by $25\text{--}50\text{ W m}^{-2}$, and latent heat flux due to evaporation by $50\text{--}100\text{ W m}^{-2}$. In July, the average enhancement in latent flux due to evaporation by cold pools is 32 W m^{-2} above the monthly mean and cold pools occur during $\sim 21\%$ of the time.

Above a viscous interfacial sublayer, the sensible (Q_{sen}) and latent (Q_{lat}) heat fluxes between the ocean and atmosphere are turbulent processes. The turbulent air–sea fluxes depend on the wind speed relative to ocean surface (S), expressed according to a bulk aerodynamic formula as

$$Q_{\text{sen}} = \rho_a c_{pa} C_h S (T_a - T_s) \quad (1a)$$

and

$$Q_{\text{lat}} = \rho_a L_e C_e S (q_a - q_s), \quad (1b)$$

where ρ_a is the air density, c_{pa} is the specific heat of air, L_e is the latent heat of evaporation, C_h and C_e are the transfer coefficients of sensible and latent heat flux, q_s is the saturated specific humidity at T_s , the sea surface temperature, and q_a and T_a are, respectively, the specific humidity and temperature of the air at a few meters above the air–sea interface (Fairall et al. 1996; Cronin and Sprintall 2001). We used the

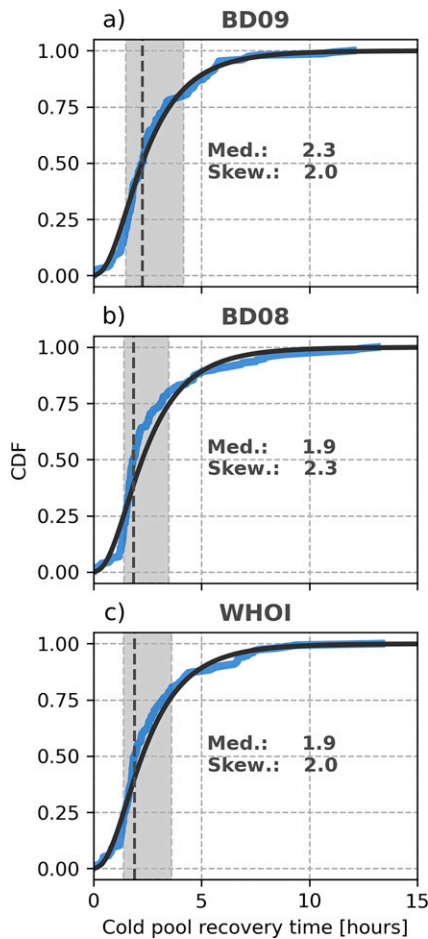


FIG. 4. Cumulative density function (CDF) for detected cold pools from (a) BD09, (b) BD08, and (c) WHOI. The dark gray dashed line represents the median, and the shaded gray area represents the 20–80th-percentile range. The dark gray solid line represents the lognormal fit for all moorings.

sign convention that negative fluxes tend to cool and/or evaporate water from the ocean surface.

The latent and sensible (Figs. 5b,c) fluxes are enhanced mainly due to the anomalous thermodynamic interfacial differences of humidity ($q_a - q_s$, Fig. 5e) and temperature ($T_a - T_s$, Fig. 5f). Some cold pools even reached 4°C colder than the T_s and 7 g kg⁻¹ drier than the saturated specific humidity at q_s . We also investigate how much of this heat flux enhancement is driven by wind anomalies. The cold pools clearly intensify the wind direction and speed variability but, after the front, do not necessarily increase the mean wind speed. Some of the cold pools show an increase and others even show a decrease in wind speed (Fig. 5d).

The near-surface air temperature outside cold pools is usually higher than the sea surface temperature in July. The resulting reversed (warming the ocean) air–sea heat flux is probably an effect of horizontal heat advection and entrainment-derived heat flux from continental air above the atmospheric boundary layer, even in stable conditions where shear instabilities are not

expected to occur. This process was reported and explored in detail by Bhat and Fernando (2016) during Indian summer monsoon.

The occurrence of cold pools in the north bay has a strong seasonal and diurnal variability (Fig. 6a). Most of the cold pools occur in the summer monsoon. They also preferentially occur in the daytime, specifically in the late morning. To explore their occurrence with rain, we also present a joint histogram of cold pools and total rain (Fig. 6b). The most intense rain events happen in the early summer monsoon (June–July), usually from midnight to sunset, and winter monsoon rainfall is weaker and restricted to daytime. Except for the winter monsoon, the joint histograms for the rain and cold pool events present practically the same pattern (Fig. 6), showing a strong relationship between the occurrence of cold pools and the rainfall in the Bay of Bengal.

One possible explanation for the diurnal cycle in the cold pools occurrence is the southward propagating monsoon storms reaching different latitudes at different times in the Bay of Bengal (Zuidema 2003). Joseph et al. (2021) observed that most of the cold pools occur in the afternoon for a mooring located at 15°N, which explains the earlier peak in the cold pools and rain events in the data we are analyzing, as the moorings are approximately 3° north of the northernmost mooring they investigate. Our results match the rain variability described by Sahany et al. (2010), Jain et al. (2018), and Webster et al. (2002) of these southward propagating storms, peaking in the late morning (1130 local time) for the north bay. Furthermore, the moorings we analyzed could also be affected by the land–sea breeze circulations (Kilpatrick et al. 2017).

6. Composites of cold pools

Some of the analyses presented in the last section are sample case studies, and to statistically investigate the role of the wind and other characteristics of cold pools, we present cold pool composites (median and range of 20th–80th percentiles) and prominence scatterplots for different anomalous physical properties (Figs. 7 and 8).

As cold pools can substantially vary in duration (Fig. 4), we normalized the time axis by the recovery time, where t_0 is the maximum of temperature before the cold pool front, t_d is the time of the negative peak of temperature and 1 is t_d plus the recovery time. Hence, all cold pools are stretched in time, comprising from t_0 to 1 (Fig. 7).

The composite for air temperature shows that 80% of all cold pools reach at least 1°C temperature drop and at least 50% of the cold pools reach at least 2°C temperature drop with a wide spread, as many events could reach >3°C, mostly during the summer (Fig. 8a). Figures 8b and 8c show the sensible and latent heat fluxes and the fluxes computed with a low-pass wind and low-pass temperature and humidity. We computed the low-pass series by a 3-day running average, considering that some of the stacked cold pools—complexes of multiple cold pools—can last a whole day. Thus, the low-pass composites aim to remove the variability related to cold pools in the wind or in the temperature and humidity.

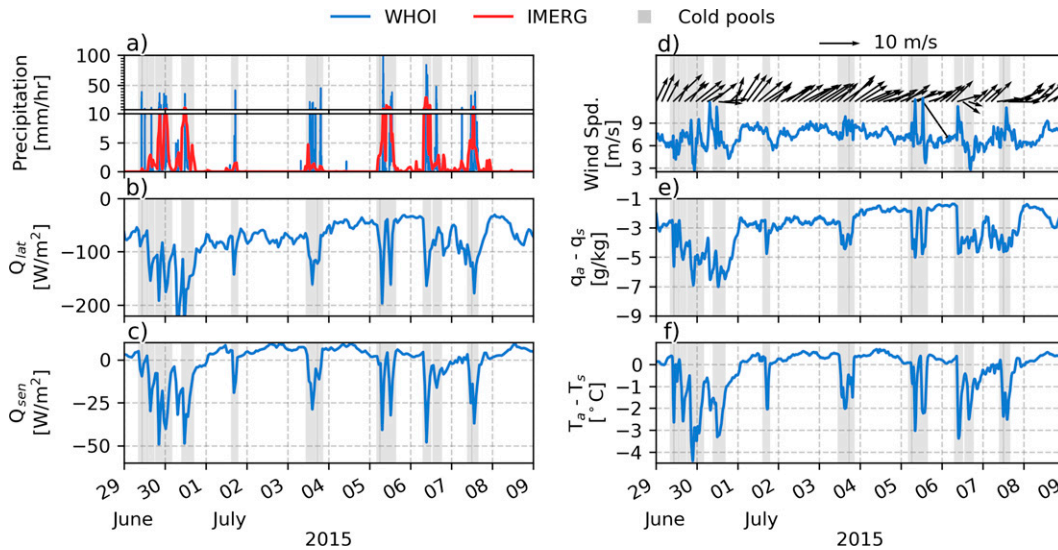


FIG. 5. (a) WHOI mooring precipitation, (b) latent heat flux, (c) sensible heat flux, (d) wind velocity data, (e) interfacial difference of humidity, and (f) temperature. Negative values in (e) and (f) stand for dry and cold air, respectively. The red line depicts the precipitation rate from IMERG for the closest gridpoint to the mooring.

As reported by Joseph et al. (2021), our analysis suggests that the wind is responsible for only 10% of the cold pool sensible heat flux enhancement in the Bay of Bengal, with at least 50% of events peaking at 16 W m^{-2} below base level (Fig. 7b). The summer events can enhance the sensible and latent heat fluxes higher than 25 and 50 W m^{-2} , respectively (Figs. 8b,c). Contrasting with the results presented by Joseph et al. (2021), our cold pool composite for the latent heat flux suggests that the wind is only responsible for 9% of the enhancement in the evaporation (Fig. 7c). While this is

considerably smaller than the result from the previous study (40%–60%; Joseph et al. 2021), their study has also shown that the wind contribution tends to decrease with increasing latitude. Indeed, the wind speed distribution is very wide and variable, and just as expected from the study cases (Fig. 5) and the surface flux composites, it increases for some events and decreases for others. Even so, the wind speed seems to increase more often than decrease, as at least half of the events peak at 0.8 m s^{-1} close to the air temperature drop (Fig. 7d). On the other hand, the 3-h running standard deviation of the wind speed and direction clearly depict the gust front at the edge of cold pools (Figs. 7e,f). In particular, the wind direction varies at least 6° for half of cold pools and more than 18° for 20% of cold pools. In other words, the wind stress becomes more variable, but not necessarily stronger during cold pools in the north bay. Nevertheless, cold pools in the north of the Bay of Bengal are colder, but less windy than the equatorial cold pools analyzed by de Szoek et al. (2017), consistent with the latitudinal variability presented in Joseph et al. (2021).

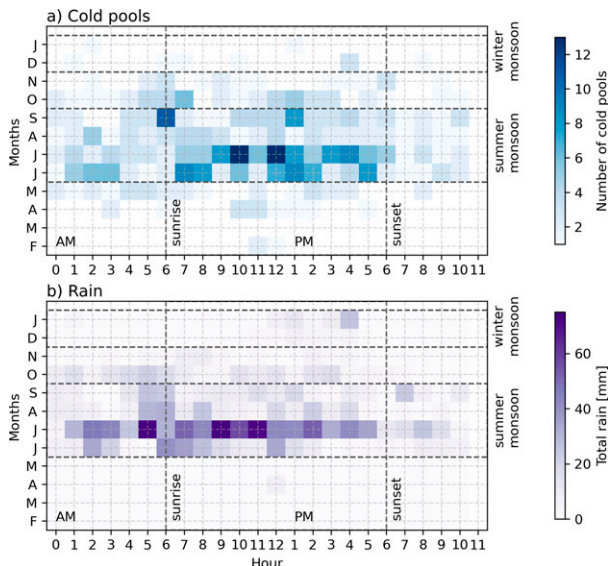


FIG. 6. Joint histogram of (a) cold pools' occurrence and (b) total rain. The x axis represents hours of the day and the y axis represents months.

Reinforcing the discussion from previous sections, the rain is clearly correlated with cold pools, with 50% of the events peaking above 3 mm h^{-1} , and 20% of stronger events peaking above 12 mm h^{-1} (Fig. 7g). Summer events can reach more than 40 mm h^{-1} (Fig. 8g). However, there is no rain for 20% of identified cold pools, indicating its high variability. One possible explanation for this variability is that the rain can evaporate completely before reaching the ocean surface and still generate a cold pool. Another explanation is that some cold pools may spread out beyond the rain shower and downdraft that generates them.

Both sea surface temperature (SST) and sea surface salinity (SSS) gently follow the drop of air temperature with a larger spread in their distribution (Figs. 7h,i). In particular, the SSS

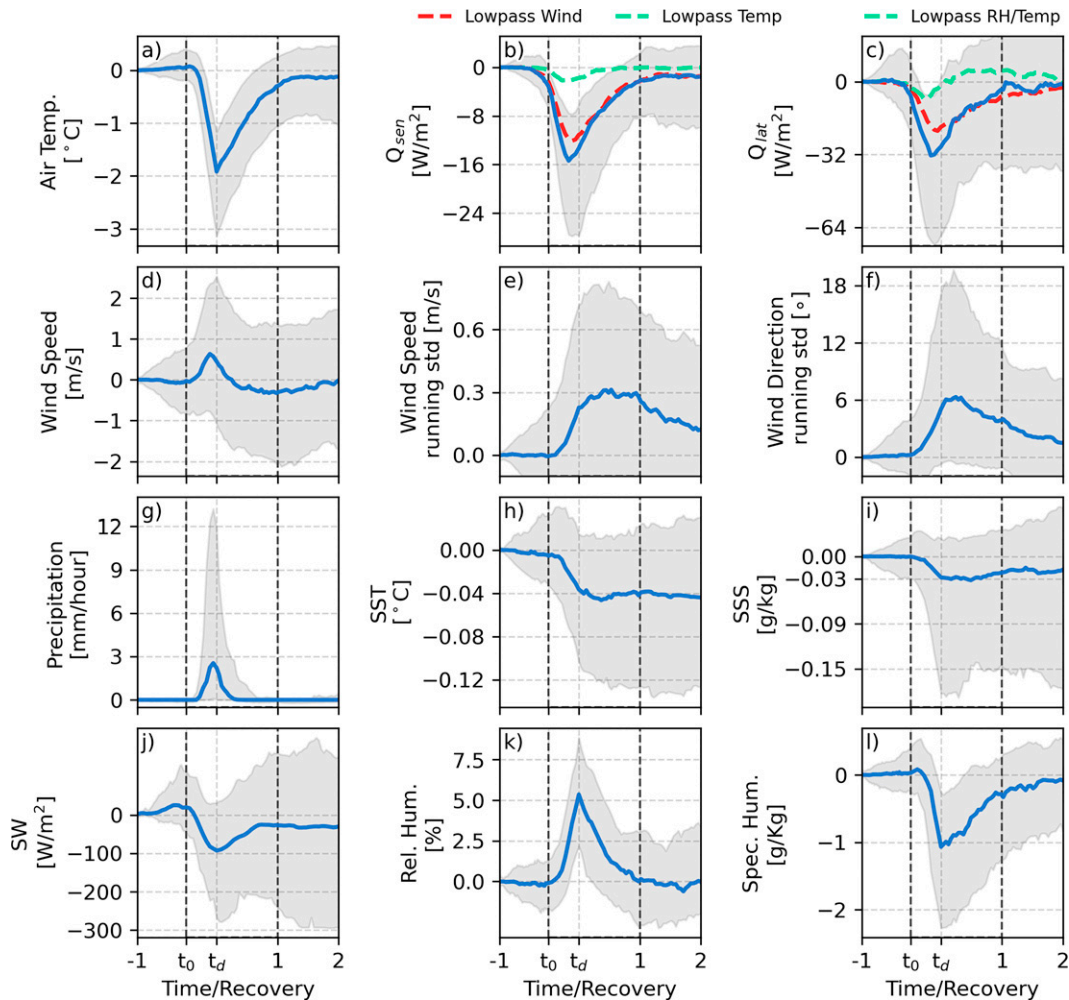


FIG. 7. Composite for 50th-percentile anomalous (a) air temperature, (b) sensible heat flux, (c) latent heat flux, (d) wind speed, (e) wind speed 3-h running standard deviation, (f) wind direction 3-h running standard deviation, (g) rain rate, (h) sea surface temperature, (i) sea surface salinity, (j) shortwave radiation, (k) relative humidity, and (l) specific humidity. The time axis is normalized by the recovery time, where t_0 is the beginning of cold pools, t_d is the time of the negative peak of temperature, and 1 is t_d plus the recovery time. The shaded gray area represents the 20–80th-percentile range. Also shown in (b) and (c) are the sensible and latent heat fluxes computed with a 3-day running-average wind (red) and temperature and humidity (green).

may be strongly influenced by precipitation, with a strong negative skewness and more than 20% of the events dropping more than 0.1 g kg^{-1} . Interestingly, the SST and SSS drops are higher from September to November, when the cold pools are less cold and gusty, reaching $>0.2^\circ\text{C}$ and $>0.5 \text{ g kg}^{-1}$ (Figs. 8h,i). Though some of this variability is likely due to salinity changes associated with river water advection (Sree Lekha et al. 2018, 2020), most of SSS drop is probably due to rain-formed fresh lenses (Wijsekera et al. 1999; Asher et al. 2014). These fresh lenses can persist for hours and extend 40 m below—depending on the wind stress—and are usually related to critical Richardson numbers, suggesting shear instability generates turbulent mixing in the lenses (Wijsekera et al. 1999; Iyer and Drushka 2021). Recently, Girishkumar et al. (2021) investigated the role of atmospheric

cold pools on the SST in the Bay of Bengal. Their study describes that most of the cooling occurs due to the wind-driven mixing of the diurnal warm layer during the afternoon. The SST drops we observe in the north bay are smaller than those observed from 8° to 15°N (Girishkumar et al. 2021), this latitudinal difference could be explained by the fact that cold pools are less gusty and occur earlier in the north, when the diurnal warm layer is not fully developed.

The shortwave radiation during cold pool events presents a wide distribution (Fig. 7j), probably due to the variability shown by the precipitation composite, but it still drops at least 100 W m^{-2} from the mean at the peak of precipitation for half of the cold pools, probably due to higher cloud coverage. Indeed, summer events can decrease the shortwave radiation 600 W m^{-2} (Fig. 8j). The positive peak in the relative

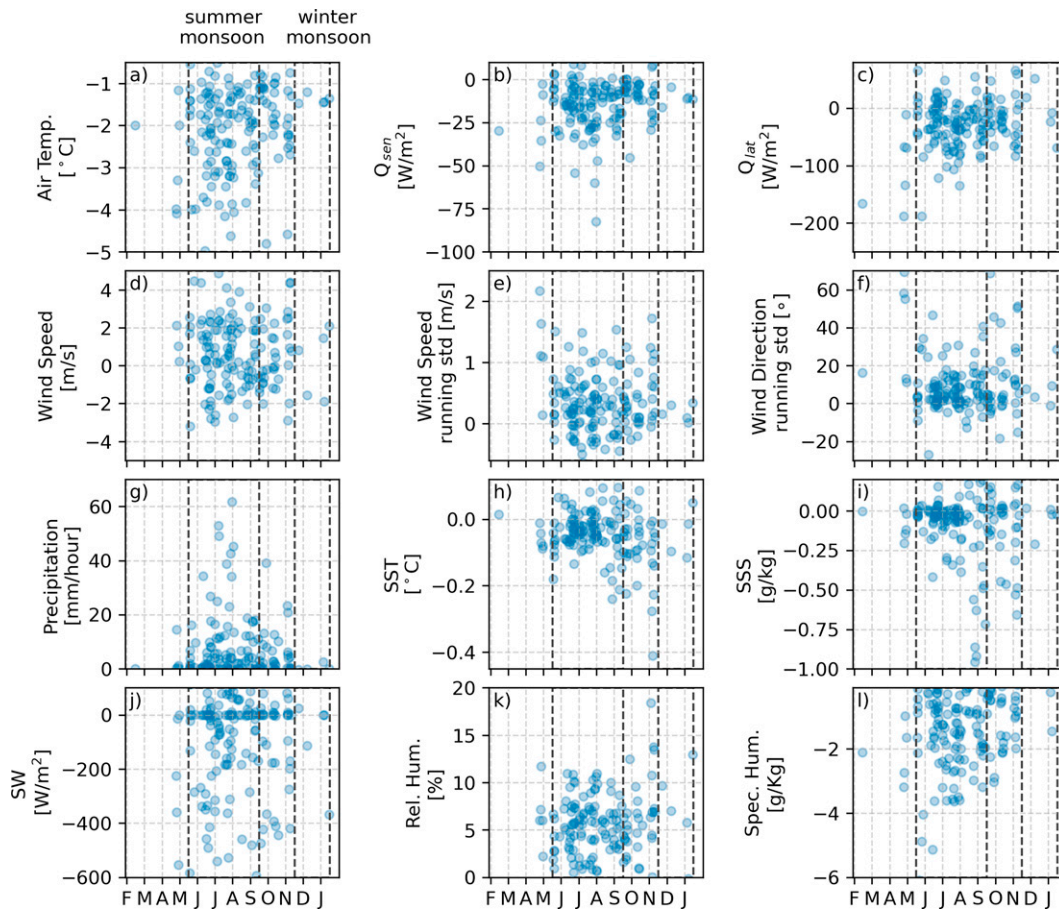


FIG. 8. Scatterplot of prominence for the anomaly ($t_d - t_0$) of each of the variables: (a) air temperature, (b) sensible heat flux, (c) latent heat flux, (d) wind speed, (e) wind speed 3-h running standard deviation, (f) wind direction 3-h running standard deviation, (g) rain rate, (h) sea surface temperature, (i) sea surface salinity, (j) shortwave radiation, (k) relative humidity, and (l) specific humidity.

humidity occurs due to the air temperature drop. The specific humidity indicates all detected cold pools are drier than their surroundings (Figs. 7k,l). For half of the events, the specific humidity drops at least 1 g kg^{-1} , and more than 20% drop at least 2 g kg^{-1} . The specific humidity rises right before the drop for some of the cold pools, which is probably related to the moist ring that has been observed in numerical simulations (Tompkins 2001; Langhans and Romps 2015; Drager et al. 2020).

The humidity of land-based cold pools depends on soil moisture, with relatively dry cold pools forming over wet soils and moist cold pools over dry soils (Drager et al. 2020). In other words, since cold pool anomalies are relative to the surface background air, we expect moister cold pools if the environment is relatively dry at the surface. We have not identified a single moist cold pool in the observations here. Over the central equatorial Indian Ocean, de Szoeke et al. (2017) also found most of the cold pools are dry. A possible explanation is that the downdrafts that are the source of the thermodynamic properties of the cold pools originate from evaporation into colder and drier air higher in the troposphere.

7. The height of cold pools

The sharp fronts with the temperature drops associated with cold pools occur in quick succession at the three different moorings. With no significant differences in the total number and distribution of recovery time between moorings, we believe that most of the cold pools were observed by all three moorings. Recent observations have shown that cold pools move at $10\text{--}20 \text{ m s}^{-1}$ (van den Heever et al. 2021; Wills et al. 2021), with no significant difference in the temperature drop for 20 km (Wills et al. 2021). Taking 34 km as the maximum distance between the analyzed moorings, a cold pool that moves at 10 m s^{-1} would take at maximum about an hour to reach another mooring (depending on the direction of front's propagation), which is shorter than the recovery time of 80% of the identified cold pools.

To estimate the propagation and height of the fronts, we first match the fronts of cold pools observed at all three moorings to estimate their propagation (Fig. 9). We found 83 matching events that represent about $\sim 53\%$ of all cold pools. In our conservative approach, a cold pool that happens at all three moorings at almost the same time is considered to be the same event. However, if a cold pool is observed at one

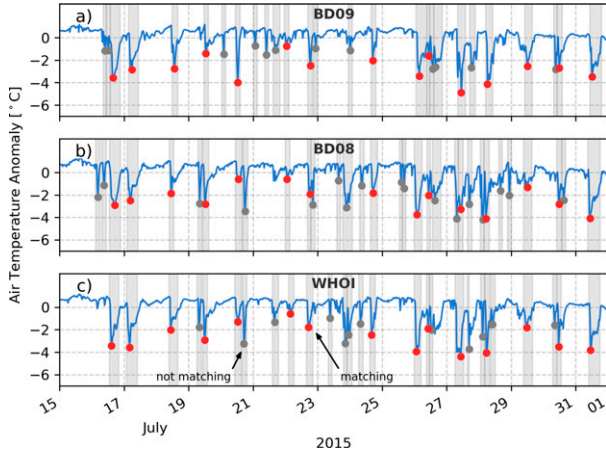


FIG. 9. Cold pool events detected by matching the air temperature anomaly at (a) BD09, (b) BD08, and (c) WHO1. Matching cold pools are marked in red.

mooring and then another one is observed at the next mooring after the first event recovers, they are taken to be two distinct events.

After matching the temperature drops at different moorings, we estimate the depth H of each cold pool just behind the front. We assume that the orientation and velocity are the same as the front crosses the moorings (frozen-field assumption), which is equivalent to a straight front that propagates along its gradient. We here define propagation as the combination of advection and phase (gust-front) components. We then approximate the gust-front speed to the linear nondispersive wave speed in shallow water $c = \sqrt{g(\Delta T/T)H}$ (e.g., chapter 5 in Gill 1982), where g is the acceleration due to gravity (9.82 m s^{-2}), ΔT is the maximum temperature drop among the moorings, T is the reference temperature (before the temperature drop), and H is the height of the gravity plume. From the gust-front speed c , we thus estimate H . Cold pools do not always satisfy the conditions of shallow-water linear gravity currents (Ross et al. 2004; Romps and Jeevanjee 2016; Borque et al. 2020). Despite the nonlinearity of the hydraulic jump, we assume the gust-front speed c is set by the speed of linear gravity waves propagating behind the nose.

We solve for the propagation velocity vector by using the time delay of matching fronts and the mooring geometry (Fig. 10a). We first estimate the angle of propagation θ by

$$\tan \theta = \frac{[(t_2 - t_0)D_{1x} - (t_1 - t_0)D_{2x}]}{[(t_1 - t_0)D_{2y} - (t_2 - t_0)D_{1y}]}, \quad (2)$$

then from θ to obtain

$$|\mathbf{V}_p| = \frac{D_{1x} \cos \theta + D_{1y} \sin \theta}{t_1 - t_0} = \frac{D_{2x} \cos \theta + D_{2y} \sin \theta}{t_2 - t_0}. \quad (3)$$

Here t_i is the time of the temperature drop at mooring i , D_{ix} is the zonal distance, and D_{iy} is the meridional distance between mooring i and mooring zero—the first the front crosses. To minimize the error associated with matching the cold pools, we only kept the cold pools that lasted at least twice

the time it took to cross the maximum distance between the moorings (40 events). Next, we estimate the gust-front speed c by subtracting the background wind velocity from the front propagation velocity (Fig. 10b). Finally, we obtain the height of the plume by $H = c^2/(g\Delta T/T)$.

Most of the fronts propagate south and southeastward at $8\text{--}20 \text{ m s}^{-1}$ (Fig. 10c), which is consistent with the southeastward propagation of diurnally evolving rainfall that generates cold pools in the Bay of Bengal (Joseph et al. 2021). That means that fronts propagate in the same direction of the cloud layer as described by previous observations (Wilbanks et al. 2015).

With most cold pools occurring during the summer under northeastward winds, some of the gravity currents go southwestward (Fig. 10d). The distribution of the maximum temperature drop of the matching cold pools is predominantly lognormal (Fig. 11a), with a median of around 1.5 K and 60% of the data between 0.9 and 2.7 K (20th–80th percentiles). The gust-front speed is more Gaussian, with a median of around 11 m s^{-1} and 60% of the data between 7 and 15.5 m s^{-1} (Fig. 11b). The gust-front speed is lower than the propagation speed of the cold pools’ parent storm (23 m s^{-1} ; Joseph et al. 2021).

The estimated cold pools’ height has a median of around 1500 m, and 60% of the data between 700 and 3100 m (Fig. 11c). There is no correlation between the gust-front speed and temperature drop (Fig. 11d). We also investigate the seasonality of the occurrence of the distribution of cold pools’ height (Fig. 11e). The group of shortest cold pools ($<850 \text{ m}$) does not present any particular seasonality, but the tallest cold pool fronts occur primarily during the summer (May–July) and September. The lifting condensation level is the level by which the air parcel becomes saturated by the water vapor and is often used to estimate the cloud-base height. Most of the observed cold pools are taller and unrelated to the lifting condensation level (90–500 m, Fig. 11f) estimated right before each front (method described by Romps 2017), which means that they can mechanically lift the surrounding air higher than the cloud-base level, reinitiating convection.

Next, we decompose the average wind anomaly at the temperature drop into along- and cross-front directions (Figs. 12a,b). As expected by the cold pool’s short duration and spatial scale, the cold pool front is not geostrophically adjusted and hence the alongfront wind anomaly does not correlate with the gust-front speed. The cross-front wind anomaly, on the other hand, correlates with gust-front speed despite being substantially weaker. The linear slope of the surface wind speed U to the gust-front speed is $U/c \approx 0.2$. In other words, stress at the surface and at the top of the gravity plume appears to slow down the wind. This frictional slowing of the surface wind is also observed for land-based cold pools (van den Heever et al. 2021).

As explained in the introduction, cold pools are problematic and expensive to survey, especially over the ocean. Unfortunately, only a few studies have addressed the height of cold pools, mostly over short time ranges of land-based events (Table 1). The values described by the present study reveal that the cold pools in the Bay of Bengal captured by this set

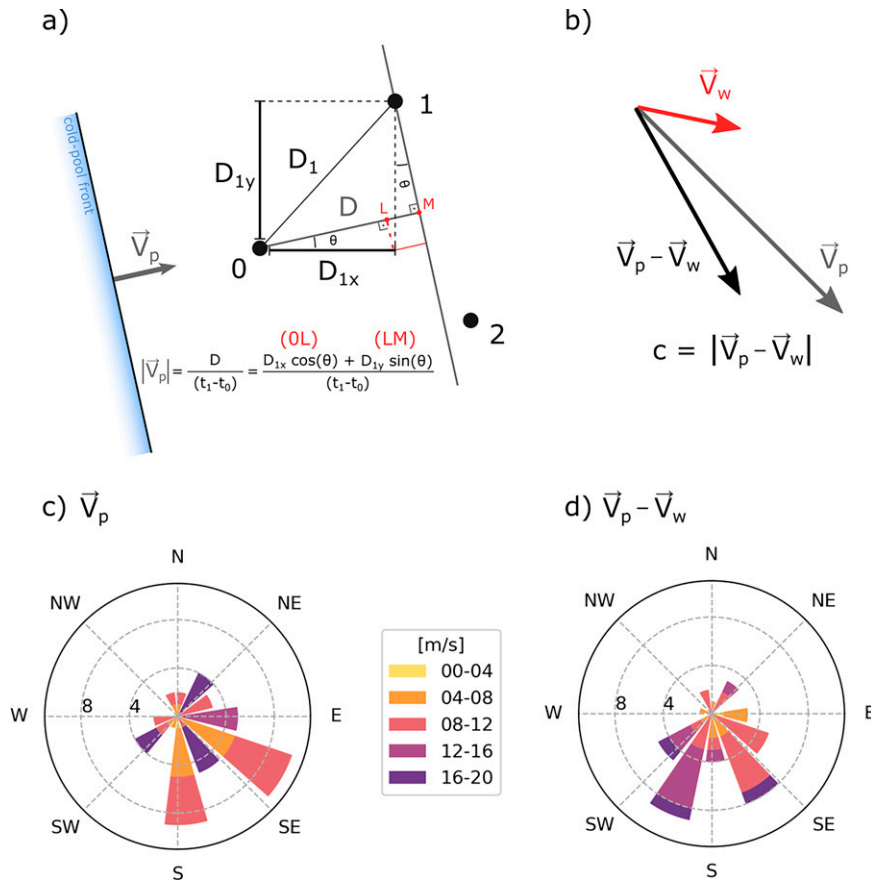


FIG. 10. (a) Schematic diagram showing method for obtaining the propagation velocity of the front. (b) Gust-front velocity is obtained by subtracting the wind velocity (\mathbf{V}_w) from the propagation velocity (\mathbf{V}_p). Polar stacked histogram for (c) \mathbf{V}_p and (d) $\mathbf{V}_p - \mathbf{V}_w$.

of closely spaced moorings could be as tall as land-based cold pools (van den Heever et al. 2021; Borque et al. 2020). Do we expect taller cold pools in larger cloud shields? Roca et al. (2017, see Fig. 14) show that the size of the cloud shield for long-lived mesoscale convective systems is unusually large in the summertime Bay of Bengal.

Our results depend on several caveats. While frozen-field assumption is not necessarily true, the time delay between matched cold pools is mostly shorter than the temperature drop duration. The matching of the cold pools is a crucial assumption for their height estimation. We note that the correlation for the temperature drop and recovery time between matching events is 0.72 and 0.74, respectively, which means we are matching not only cold pools that occur simultaneously, but with the similar characteristics. In addition, the fact that most of the fronts propagate in the same direction as the parent storm (Joseph et al. 2021) is also a good indication that we are matching the same cold pools.

8. Conclusions

In this study, we characterize a total of 465 cold pools in an array of three closely spaced moorings in the northern Bay of

Bengal for 2015. The cold pools are all dry, with a typical temperature drop of 2°C (maximum = 5°C), specific humidity drop of 1 g kg^{-1} (maximum = 6 g kg^{-1}), and recovery time of 1.5–3.5 h, with some events lasting as long as 10 h. From late April to November, cold pools appear practically every day in the north bay, primarily in the late morning, and are associated with significant precipitation, which accounts for 80% of total rainfall. Indeed, the early-July plots (Fig. 5) and the composite analysis (Fig. 7) present strong precipitation anomalies right at the front (at the temperature drops), which corroborates with the theory of the mechanical lifting and thermodynamic explanation of the rain at the leading edge of the gravity plumes. This result confirms that the temperature drops are important classifiers for rain in the Bay of Bengal (Shesu et al. 2022). However, without a method to distinguish between rainfall from cold pools' parent storms and rainfall from new storms caused by cold pools, we can only conclude association, and not necessarily causality between rainfall and cold pools.

Temperature and specific humidity anomalies within cold pools account for around $\sim 90\%$ of the increase in sensible and latent heat flux, whereas variations in wind speed account for of the rest. Individual cold pools can

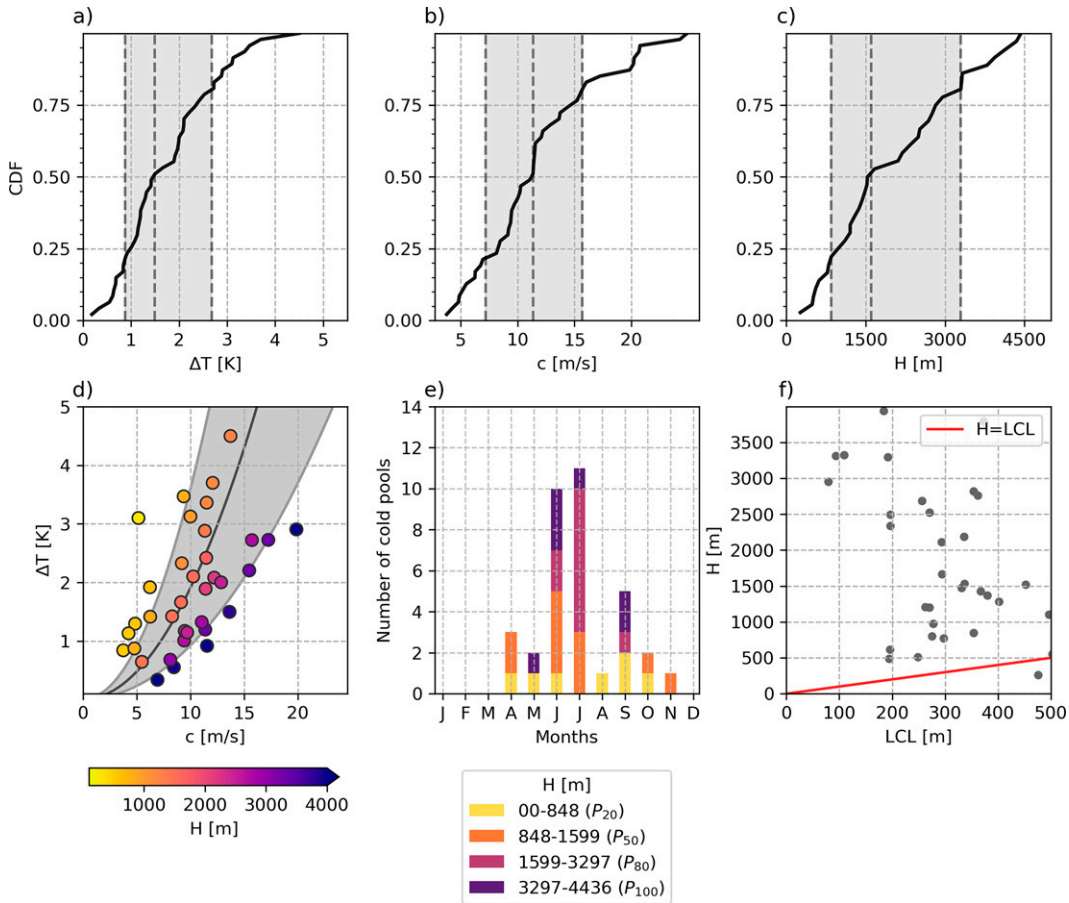


FIG. 11. Cumulative density function for (a) temperature drop (ΔT), (b) gust-front speed (c), and (c) height of the cold pool front (H). (d) Scatterplot of temperature drop and gust-front speed. Colors represent the height of the leading edge of the cold pools. The gray shaded area in (a)–(d) represent the range between the 20th and 80th percentiles. (e) Stacked histogram of the occurrence of cold pools for different percentile ranges. (f) Comparison between height of cold pools and lifting condensation level.

increase latent heat flux by up to 150 W m^{-2} , and we estimate that cold pools account for almost 14% of total evaporation in the rainiest month (July). Based on propagation speed, the predicted height of the cold pools

has a lognormal distribution, predominantly spanning from 850 to 3200 m. Taller cold pools are more likely to develop during June–September’s summer monsoon season.

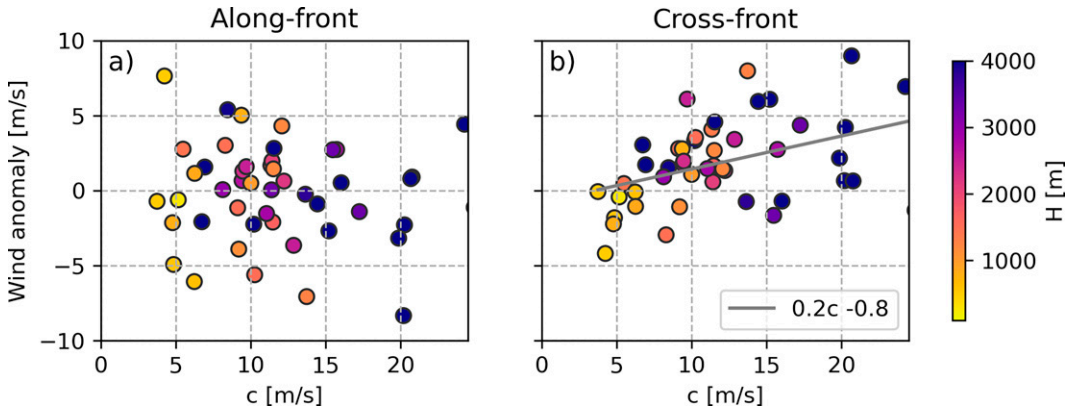


FIG. 12. (a) Alongfront and (b) cross-front wind anomaly against gust-front speed of the cold pools’ fronts. Color shading represent the estimated height of the cold pools.

TABLE 1. Some previous studies on the height of cold pool fronts.

Study	Surface	Source	Height
van den Heever et al. (2021)	Continent	Observations	200–2300 m
Borque et al. (2020)	Continent	Observations	1000–3000 m on avg (2500–4000 m max)
Drager et al. (2020)	Continent	Model	1000 m (wet soil)–1750 m (dry soil) on avg
Mallinson and Lasher-Trapp (2019)	Continent	Model	400–1500 m
de Szoek et al. (2017)	Ocean	Observations	320 m median (700 m max)
Li et al. (2014)	Continent	Model	1500–2000 m
Terai and Wood (2013)	Ocean	Observations	300 m
Dawson et al. (2010)	Continent	Model	2500 m
Roux (1988)	Continent	Observations	2500 m on avg (3500 m max)
Charba (1974)	Ocean	Observations	1700 m

The Clausius–Clapeyron relation predicts that for constant sea–air temperature difference and relative humidity, evaporation from the tropical ocean is higher when SST is higher. Our analyses show that sea–air temperature and humidity vary in such a way to violate this assumption during the South Asian summer monsoons. Air–sea exchange is influenced by cold pools 21% of the time. Cold pool transients add in average 32 W m^{-2} ($>100 \text{ W m}^{-2}$ for many events during the summer) to the local supply of moisture to the atmosphere. Cold pools are responsible for at least 14% of the July mean evaporation. A significant message is that in spite of the observed SST cooling during subseasonal rain spells, monsoon clouds actively enhance moisture flux from the ocean by creating cold pools, an important positive feedback. This has important implications for the coupled models that do not resolve the cold pools and its enhanced evaporation.

Convective clouds propagate southward in the Bay of Bengal (Zuidema 2003), with larger systems in the north bay (Roca et al. 2017). The latitudinal variability of the wind and temperature anomalies associated with cold pools as shown by Joseph et al. (2021) in combination with the present work could be related to the evolution of the parent storm as it dissipates while propagating southward.

Usually, climate models have too much convective precipitation, with a strong moisture–precipitation relationship in the equatorial Indian Ocean (e.g., Sabeerali et al. 2015). This suggests that it rains too quickly in the modeled equatorial ocean, with a lack of sufficient precipitation over the Indian landmass and north of the Bay of Bengal. The dry bias in the current reanalyses have been discussed as a consequence of a more generic problem in the parameterizations used in these models (Goswami et al. 2014). Studies have also shown a strong negative bias in the summer monsoon precipitation over the Indian landmass and the north Bay of Bengal (e.g., see Fig. 2 from Ramu et al. 2016). Most reanalyses show biases in the air–sea fluxes (Sanchez-Franks et al. 2018) due to the uncertainty or lack of parameterization of major subgrid-scale processes (Sabeerali et al. 2015; Goswami et al. 2014). Our analysis highlights the importance of cold pools for the air–sea fluxes and rainfall in the Bay of Bengal. The role of cold pools in reducing surface flux biases and the rainfall bias in climate models is a major topic that needs to be explored in future regional climate studies.

Acknowledgments. I.T.S., A.T., and J.B. acknowledge the support by Office of Naval Research under Grants N00014-17-1-2355

and N00014-19-1-2410. D.S. acknowledges support from the Indian Institute of Tropical Meteorology (IITM), Pune, under the Ministry of Earth Sciences (MoES) Delhi, through the National Monsoon Mission. S.D. acknowledges the support by Office of Naval Research under Grants N00014-16-1-3094 and N00014-22-1-2042. J.S.L. thanks the Divecha Centre for Climate Change (DCCC), National Research Council (NRC) and Pacific Marine Environmental Laboratory (PMEL; Contribution Number 5363) for support. I.T.S. thanks Igor Uchoa Farias for the help on the LCL estimates and Agata Piffer-Braga for the discussions on the estimate for the length scale of the cold pools.

Data availability statement. The dataset used in this paper are available for the public. The OMNI data are available at <http://do.incois.gov.in/> and the WHOI data are available at <http://uop.whoi.edu/projects/Bengal/QCData.html>. The IMERG data were provided by the NASA Goddard Space Flight Center and PPS, which develop and compute the IMERG as a contribution to TMPA and GPM constellation satellites, and archived at the NASA GES DISC (<https://gpm.nasa.gov/data>).

REFERENCES

- Asher, W. E., A. T. Jessup, R. Branch, and D. Clark, 2014: Observations of rain-induced near-surface salinity anomalies. *J. Geophys. Res. Oceans*, **119**, 5483–5500, <https://doi.org/10.1002/2014JC009954>.
- Bhat, G. S., and H. J. S. Fernando, 2016: Remotely driven anomalous sea-air heat flux over the north Indian Ocean during the summer monsoon season. *Oceanography*, **29** (2), 232–241, <https://doi.org/10.5670/oceanog.2016.55>.
- Black, P. G., 1978: Mesoscale cloud patterns revealed by Apollo-Soyuz photographs. *Bull. Amer. Meteor. Soc.*, **59**, 1409–1419, [https://doi.org/10.1175/1520-0477\(1978\)059<1409:MCPRBA>2.0.CO;2](https://doi.org/10.1175/1520-0477(1978)059<1409:MCPRBA>2.0.CO;2).
- Borque, P., S. W. Nesbitt, R. J. Trapp, S. Lasher-Trapp, and M. Oue, 2020: Observational study of the thermodynamics and morphological characteristics of a midlatitude continental cold pool event. *Mon. Wea. Rev.*, **148**, 719–737, <https://doi.org/10.1175/MWR-D-19-0068.1>.
- Charba, J., 1974: Application of gravity current model to analysis of squall-line gust front. *Mon. Wea. Rev.*, **102**, 140–156, [https://doi.org/10.1175/1520-0493\(1974\)102<0140:AOGCMT>2.0.CO;2](https://doi.org/10.1175/1520-0493(1974)102<0140:AOGCMT>2.0.CO;2).
- Cherian, D. A., E. L. Shroyer, H. W. Wijesekera, and J. N. Moum, 2020: The seasonal cycle of upper-ocean mixing at

- 8°N in the Bay of Bengal. *J. Phys. Oceanogr.*, **50**, 323–342, <https://doi.org/10.1175/JPO-D-19-0114.1>.
- Cronin, M. F., and J. Sprintall, 2001: Wind and buoyancy-forced Upper Ocean. *Encyclopedia of Ocean Sciences*, J. H. Steele, Ed., Academic Press, 3219–3226, <https://doi.org/10.1006/rwos.2001.0157>.
- Dawson, D. T., M. Xue, J. A. Milbrandt, and M. K. Yau, 2010: Comparison of evaporation and cold pool development between single-moment and multimoment bulk microphysics schemes in idealized simulations of tornadic thunderstorms. *Mon. Wea. Rev.*, **138**, 1152–1171, <https://doi.org/10.1175/2009MWR2956.1>.
- de Szoeke, S. P., E. D. Skyllingstad, P. Zuidema, and A. S. Chandra, 2017: Cold pools and their influence on the tropical marine boundary layer. *J. Atmos. Sci.*, **74**, 1149–1168, <https://doi.org/10.1175/JAS-D-16-0264.1>.
- Drager, A. J., L. D. Grant, and S. C. van den Heever, 2020: Cold pool responses to changes in soil moisture. *J. Adv. Model. Earth Syst.*, **12**, e2019MS001922, <https://doi.org/10.1029/2019MS001922>.
- Edson, J. B., and Coauthors, 2013: On the exchange of momentum over the open ocean. *J. Phys. Oceanogr.*, **43**, 1589–1610, <https://doi.org/10.1175/JPO-D-12-0173.1>.
- Fairall, C. W., E. F. Bradley, D. P. Rogers, J. B. Edson, and G. S. Young, 1996: Bulk parameterization of air-sea fluxes for Tropical Ocean-Global Atmosphere Coupled-Ocean Atmosphere Response Experiment. *J. Geophys. Res.*, **101**, 3747–3764, <https://doi.org/10.1029/95JC03205>.
- , —, J. E. Hare, A. A. Grachev, and J. B. Edson, 2003: Bulk parameterization of air-sea fluxes: Updates and verification for the COARE algorithm. *J. Climate*, **16**, 571–591, [https://doi.org/10.1175/1520-0442\(2003\)016<0571:BPOASF>2.0.CO;2](https://doi.org/10.1175/1520-0442(2003)016<0571:BPOASF>2.0.CO;2).
- Gill, A. E., 1982: *Atmosphere–Ocean Dynamics*. Vol. 30. Academic Press, 662 pp.
- Girishkumar, M. S., J. Joseph, M. J. McPhaden, and E. Pattabhi Ram Rao, 2021: Atmospheric cold pools and their influence on sea surface temperature in the Bay of Bengal. *J. Geophys. Res. Oceans*, **126**, e2021JC017297, <https://doi.org/10.1029/2021JC017297>.
- Goff, R. C., 1976: Vertical structure of thunderstorm outflows. *Mon. Wea. Rev.*, **104**, 1429–1440, [https://doi.org/10.1175/1520-0493\(1976\)104<1429:VSOTO>2.0.CO;2](https://doi.org/10.1175/1520-0493(1976)104<1429:VSOTO>2.0.CO;2).
- Goswami, B. B., M. Deshpande, P. Mukhopadhyay, S. K. Saha, S. A. Rao, R. Murthugudde, and B. N. Goswami, 2014: Simulation of monsoon intraseasonal variability in NCEP CFSv2 and its role on systematic bias. *Climate Dyn.*, **43**, 2725–2745, <https://doi.org/10.1007/s00382-014-2089-5>.
- Goswami, B. N., S. A. Rao, D. Sengupta, and S. Chakravorty, 2016: Monsoons to mixing in the Bay of Bengal: Multiscale air-sea interactions and monsoon predictability. *Oceanography*, **29** (2), 18–27, <https://doi.org/10.5670/oceanog.2016.35>.
- Grant, L. D., and S. C. van den Heever, 2016: Cold pool dissipation. *J. Geophys. Res. Atmos.*, **121**, 1138–1155, <https://doi.org/10.1002/2015JD023813>.
- Iyer, S., and K. Drushka, 2021: Turbulence within rain-formed fresh lenses during the SPURS-2 experiment. *J. Phys. Oceanogr.*, **51**, 1705–1721, <https://doi.org/10.1175/JPO-D-20-0303.1>.
- Jain, D., A. Chakraborty, and R. S. Nanjundiah, 2018: A mechanism for the southward propagation of mesoscale convective systems over the Bay of Bengal. *J. Geophys. Res. Atmos.*, **123**, 3893–3913, <https://doi.org/10.1002/2017JD027470>.
- Jeevanjee, N., 2017: Vertical velocity in the gray zone. *J. Adv. Model. Earth Syst.*, **9**, 2304–2316, <https://doi.org/10.1002/2017MS001059>.
- Joseph, J., M. S. Girishkumar, M. J. McPhaden, and E. P. R. Rao, 2021: Diurnal variability of atmospheric cold pool events and associated air-sea interactions in the Bay of Bengal during the summer monsoon. *Climate Dyn.*, **56**, 837–853, <https://doi.org/10.1007/s00382-020-05506-w>.
- Kilpatrick, T., S.-P. Xie, and T. Nasuno, 2017: Diurnal convection-wind coupling in the Bay of Bengal. *J. Geophys. Res. Atmos.*, **122**, 9705–9720, <https://doi.org/10.1002/2017JD027271>.
- Langhans, W., and D. M. Romps, 2015: The origin of water vapor rings in tropical oceanic cold pools. *Geophys. Res. Lett.*, **42**, 7825–7834, <https://doi.org/10.1002/2015GL065623>.
- Li, Z., P. Zuidema, and P. Zhu, 2014: Simulated convective invigoration processes at trade wind cumulus cold pool boundaries. *J. Atmos. Sci.*, **71**, 2823–2841, <https://doi.org/10.1175/JAS-D-13-0184.1>.
- Llobera, M., 2001: Building past landscape perception with GIS: Understanding topographic prominence. *J. Archaeol. Sci.*, **28**, 1005–1014, <https://doi.org/10.1006/jasc.2001.0720>.
- Mallinson, H. M., and S. G. Lasher-Trapp, 2019: An investigation of hydrometeor latent cooling upon convective cold pool formation, sustainment, and properties. *Mon. Wea. Rev.*, **147**, 3205–3222, <https://doi.org/10.1175/MWR-D-18-0382.1>.
- Ramu, D. A., and Coauthors, 2016: Indian summer monsoon rainfall simulation and prediction skill in the CFSv2 coupled model: Impact of atmospheric horizontal resolution: ISMR simulation and prediction in CFSv2. *J. Geophys. Res. Atmos.*, **121**, 2205–2221, <https://doi.org/10.1002/2015JD024629>.
- Roca, R., T. Fiolleau, and D. Bouniol, 2017: A simple model of the life cycle of mesoscale convective systems cloud shield in the tropics. *J. Climate*, **30**, 4283–4298, <https://doi.org/10.1175/JCLI-D-16-0556.1>.
- Romps, D. M., 2017: Exact expression for the lifting condensation level. *J. Atmos. Sci.*, **74**, 3891–3900, <https://doi.org/10.1175/JAS-D-17-0102.1>.
- , and N. Jeevanjee, 2016: On the sizes and lifetimes of cold pools. *Quart. J. Roy. Meteor. Soc.*, **142**, 1517–1527, <https://doi.org/10.1002/qj.2754>.
- Ross, A. N., A. M. Tompkins, and D. J. Parker, 2004: Simple models of the role of surface fluxes in convective cold pool evolution. *J. Atmos. Sci.*, **61**, 1582–1595, [https://doi.org/10.1175/1520-0469\(2004\)061<1582:SMOTRO>2.0.CO;2](https://doi.org/10.1175/1520-0469(2004)061<1582:SMOTRO>2.0.CO;2).
- Roux, F., 1988: The West African squall line observed on 23 June 1981 during COPT 81: Kinematics and thermodynamics of the convective region. *J. Atmos. Sci.*, **45**, 406–426, [https://doi.org/10.1175/1520-0469\(1988\)045<0406:TWASLO>2.0.CO;2](https://doi.org/10.1175/1520-0469(1988)045<0406:TWASLO>2.0.CO;2).
- Sabeerali, C. T., S. A. Rao, A. R. Dhakate, K. Salunke, and B. N. Goswami, 2015: Why ensemble mean projection of South Asian monsoon rainfall by CMIP5 models is not reliable? *Climate Dyn.*, **45**, 161–174, <https://doi.org/10.1007/s00382-014-2269-3>.
- Sahany, S., V. Venugopal, and R. S. Nanjundiah, 2010: Diurnal-scale signatures of monsoon rainfall over the Indian region from TRMM satellite observations. *J. Geophys. Res.*, **115**, D02103, <https://doi.org/10.1029/2009JD012644>.
- Sanchez-Franks, A., E. C. Kent, A. J. Matthews, B. G. Webber, S. C. Peatman, and P. N. Vinayachandran, 2018: Intraseasonal variability of air-sea fluxes over the Bay of Bengal during the southwest monsoon. *J. Climate*, **31**, 7087–7109, <https://doi.org/10.1175/JCLI-D-17-0652.1>.
- Shesu, R. V., M. Ravichandran, K. Suprit, E. P. R. Rao, and B. V. Rao, 2022: Precipitation event detection based on air temperature over the equatorial Indian Ocean. *Indian J. Geo-Mar. Sci.*, **51**, 117–125, <https://doi.org/10.56042/ijms.v51i02.40612>.

- Sree Lekha, J., J. M. Buckley, A. Tandon, and D. Sengupta, 2018: Subseasonal dispersal of freshwater in the northern Bay of Bengal in the 2013 summer monsoon season. *J. Geophys. Res. Oceans*, **123**, 6330–6348, <https://doi.org/10.1029/2018JC014181>.
- , A. J. Lucas, J. Sukhatme, J. K. Joseph, M. Ravichandran, N. Suresh Kumar, J. T. Farrar, and D. Sengupta, 2020: Quasi-biweekly mode of the Asian summer monsoon revealed in Bay of Bengal surface observations. *J. Geophys. Res. Oceans*, **125**, e2020JC016271, <https://doi.org/10.1029/2020JC016271>.
- Terai, C. R., and R. Wood, 2013: Aircraft observations of cold pools under marine stratocumulus. *Atmos. Chem. Phys.*, **13**, 9899–9914, <https://doi.org/10.5194/acp-13-9899-2013>.
- Thakur, M. K., T. V. L. Kumar, M. S. Narayanan, K. R. Kundeti, and H. Barbosa, 2020: Analytical study of the performance of the IMERG over the Indian landmass. *Meteor. Appl.*, **27**, e1908, <https://doi.org/10.1002/met.1908>.
- Tompkins, A. M., 2001: Organization of tropical convection in low vertical wind shears: The role of cold pools. *J. Atmos. Sci.*, **58**, 1650–1672, [https://doi.org/10.1175/1520-0469\(2001\)058<1650:OOTCIL>2.0.CO;2](https://doi.org/10.1175/1520-0469(2001)058<1650:OOTCIL>2.0.CO;2).
- Torri, G., Z. Kuang, and Y. Tian, 2015: Mechanisms for convection triggering by cold pools. *Geophys. Res. Lett.*, **42**, 1943–1950, <https://doi.org/10.1002/2015GL063227>.
- van den Heever, S. C., and Coauthors, 2021: The Colorado State University Convective Cloud Outflows and Updrafts Experiment (C3LOUD-Ex). *Bull. Amer. Meteor. Soc.*, **102**, E1283–E1305, <https://doi.org/10.1175/BAMS-D-19-0013.1>.
- Webster, P. J., and Coauthors, 2002: The JASMINE pilot study. *Bull. Amer. Meteor. Soc.*, **83**, 1603–1630, <https://doi.org/10.1175/BAMS-83-11-1603>.
- Wijesekera, H. W., C. A. Paulson, and A. Huyer, 1999: The effect of rainfall on the surface layer during a westerly wind burst in the western equatorial Pacific. *J. Phys. Oceanogr.*, **29**, 612–632, [https://doi.org/10.1175/1520-0485\(1999\)029<0612:TEOROT>2.0.CO;2](https://doi.org/10.1175/1520-0485(1999)029<0612:TEOROT>2.0.CO;2).
- Wilbanks, M. C., S. E. Yuter, S. P. de Szoeke, W. A. Brewer, M. A. Miller, A. M. Hall, and C. D. Burleyson, 2015: Near-surface density currents observed in the southeast Pacific stratocumulus-topped marine boundary layer. *Mon. Wea. Rev.*, **143**, 3532–3555, <https://doi.org/10.1175/MWR-D-14-00359.1>.
- Wills, S. M., M. F. Cronin, and D. Zhang, 2021: Cold pools observed by uncrewed surface vehicles in the central and eastern tropical Pacific. *Geophys. Res. Lett.*, **48**, e2021GL093373, <https://doi.org/10.1029/2021GL093373>.
- Zipser, E. J., 1977: Mesoscale and convective-scale downdrafts as distinct components of squall-line structure. *Mon. Wea. Rev.*, **105**, 1568–1589, [https://doi.org/10.1175/1520-0493\(1977\)105<1568:MACDAD>2.0.CO;2](https://doi.org/10.1175/1520-0493(1977)105<1568:MACDAD>2.0.CO;2).
- Zuidema, P., 2003: Convective clouds over the Bay of Bengal. *Mon. Wea. Rev.*, **131**, 780–798, [https://doi.org/10.1175/1520-0493\(2003\)131<0780:CCOTBO>2.0.CO;2](https://doi.org/10.1175/1520-0493(2003)131<0780:CCOTBO>2.0.CO;2).
- , G. Torri, C. Muller, and A. Chandra, 2017: A survey of precipitation-induced atmospheric cold pools over oceans and their interactions with the larger-scale environment. *Surv. Geophys.*, **38**, 1283–1305, <https://doi.org/10.1007/s10712-017-9447-x>.